Journal of Alloys and Compounds 937 (2023) 168408

Contents lists available at ScienceDirect

Journal of Alloys and Compounds

journal homepage: www.elsevier.com/locate/jalcom

Luminescence properties of $BaMO_4$:Eu^{3+} (M: Mo or W) phosphors derived from co-precipitation reaction

Renan P. Moreira [a], Leonardo H.C. Francisco [a], Israel F. Costa [b], Helliomar P. Barbosa [c], Ercules E.S. Teotonio [d,e], Maria C.F.C. Felinto [a,*], Oscar L. Malta [f], Hermi F. Brito [b,*]

[a] Nuclear and Energy Research Institute, University of São Paulo, São Paulo, SP, Brazil
[b] Institute of Chemistry, University of São Paulo, São Paulo, SP, Brazil
[c] Federal Institute of Education, Science and Technology Goiano, Rio Verde, Goias, Brazil
[d] Department of Chemistry, Federal University of Paraíba, João Pessoa, PB, Brazil
[e] Institute of Inorganic Chemistry, Christian-Albrechts University of Kiel, Kiel, Germany
[f] Department of Fundamental Chemistry, Federal University of Pernambuco, Recife, PE, Brazil

ARTICLE INFO

Article history:
Received 19 July 2022
Received in revised form 2 December 2022
Accepted 7 December 2022
Available online 16 December 2022

Keywords:
Luminescence
Europium
Tungstate
Molybdate
Coprecipitation
Phosphor

ABSTRACT

Luminescent $BaMO_4$:xmol%Eu^{3+} materials (M: Mo or W, and x: 0, 2, 4, 6, 8, and 10 mol%) were successfully obtained by a coprecipitation method at room temperature without additional thermal treatment, leading to highly crystalline materials with reduced reaction times and low manufacturing cost. Structural analyses by powder X-ray diffraction and vibrational Raman techniques of the $[WO_4]^{2-}$ and $[MoO_4]^{2-}$ groups confirm a characteristic scheelite-type structure. The results indicate an average crystallite size at around 30 nm, and a highly pure phase has been supported by Rietveld refinement. SEM-EDS data of $BaMO_4$:xmol%Eu^{3+} materials identified polycrystalline particles with bipyramidal-like morphology and homogeneous europium ion distribution. Additionally, the band gap energy (E_g) of barium molybdate and tungstate materials were calculated from reflectance data by the single-constant Kubelka-Munk function. Furthermore, the emission intensity, lifetime, and intrinsic emission quantum yield ($Q_{Eu^{3+}}^{Eu^{3+}}$) of the materials have been determined and discussed. The luminescent properties of these materials are significantly influenced by the LMCT excitation bands ($O^{2-} \rightarrow Mo^{6+}$, W^{6+}, and Eu^{3+}) as well as their intense red emission bands assigned to Eu^{3+} transitions. The experimental intensity parameter values Ω_2 and Ω_4 were evaluated from the emission spectra, using the magnetic dipole $^5D_0 \rightarrow {}^7F_1$ transition as the standard reference. It was observed that the Ω_2 values are much higher than the Ω_4 values. This result is related to the fact that the $^5D_0 \rightarrow {}^7F_2$ transition presents a much higher intensity than $^5D_0 \rightarrow {}^7F_1$ one suggesting a low local symmetry around the Eu^{3+} ion, which might be due to angular distortions in the local coordination geometry. The high $Q_{Eu^{3+}}^{Eu^{3+}}$ values (60–79%) indicated an overall high emission intensity for the prepared phosphors. These are special photonic features of the Eu^{3+}-doped molybdate and tungstate, suggesting they could be suitable for luminescent materials applications.

1. Introduction

Nowadays, trivalent lanthanides (Ln^{3+}) doped phosphors are among the most studied materials due to their unique optical and magnetic properties derived from the 4f–4f electronic transitions [1]. They are attractive for several technological applications such as bioimaging, photodynamic therapy, optical sensing, catalysis, lighting, and displays [2–5]. Since the 4f electrons interact weakly with the surrounding chemical environment, electronic spectra of Ln^{3+}-doped compounds exhibit characteristics like narrow absorption, excitation, and emission bands derived from forbidden intraconfigurational 4f transitions (Laporte rule, $\Delta\ell = \pm 1$) [6].

Molybdate and tungstate inorganic matrices doped with Ln^{3+} or transition metal ions may present remarkable optical properties for different applications in photocatalysis, electroluminescence devices, and photomorphogenesis greenhouse horticulture [7–11]. Moreover, Yb^{3+}/Er^{3+}-activated upconversion lanthanum tungstate-based host matrices were recently investigated as promising

* Corresponding authors.
E-mail addresses: mfelinto@ipen.br (M.C.F.C. Felinto), hefbrito@iq.usp.br (H.F. Brito).

https://doi.org/10.1016/j.jallcom.2022.168408
0925-8388/

candidates for optical thermometry and fluorescent and anticancer agents [12]. In addition, high red emission $La_{10}W_{22}O_{81}$:Eu^{3+} microphosphor rods for noncytotoxic latent fingerprint imaging have also been reported [13].

Thus, understanding the optical features of lab-scale nanophosphors is essential for developing targeted materials for novel lighting applications to obtain high luminescence efficiency. These host materials with divalent cations belong to the tetragonal space group I41/a, in which Mo^{6+} and W^{6+} ions in the molybdate $[MoO_4]^{2-}$ and tungstate $[WO_4]^{2-}$ groups are coordinated by four oxygen atoms, presenting relatively stable tetrahedral (T_d) symmetry [14–16]. For lanthanide-doped materials, it is highlighted that dopant concentration does not follow *Vegard's Law*, which states that to form a solid solution, the cations of two compounds must have ionic radii within 15% of each other. As the ratio of ionic radii values of Eu^{3+} and Ba^{2+} is close to 30%, several structural distortions may occur with increasing Eu^{3+} content. However, phase segregation in Eu^{3+}-rich $BaMO_4$ materials (M: Mo or W) is not commonly observed. Moreover, it was observed that the charge compensation effect involved the substitution of Ba^{2+} by the Eu^{3+} ion. In these materials, Ba^{2+} sites are occupied by Eu^{3+}, leading to barium vacancies or Na^{+} precursor ions act in the charge compensation effect [17].

Interestingly, the use of the inorganic host matrices with strong absorption in the ultraviolet (UV) region, which occurs commonly via excitation under Ligand-to-Metal Charge Transfer (LMCT) absorption bands, is a usual approach to improve the luminescence intensities from the Ln^{3+} materials [18]. Photoluminescence behavior of undoped $BaMO_4$ host matrices (M: Mo and W) often has shown the strong and broad absorption bands in the spectral range from 250 to 300 nm assigned to $O^{2-}(2p) \rightarrow M^{6+}(5d)$ LMCT transitions, presenting a broad emission band at around 500 nm originating the from $[MO_4]^{2-}$ groups [17,19,20]. On the other hand, Eu-doped $BaMO_4$ materials are known to display intense red emissions arising from the (Eu^{3+}) $^5D_0 \rightarrow {}^7F_2$ transition under excitations at LMCT bands and direct on 4f–4 f transitions of the lanthanide ion [16,17,21,22].

It is worth mentioning that the Eu^{3+} ion can be used as a spectroscopic probe due to its non-degenerate first emitting energy level ($^5D_0$) and ground state ($^7F_0$) as well as long lifetimes (ms). These optical features simplify spectral interpretation to suggest the point group symmetry around the Eu^{3+} chemical environment [16,23], leading to a luminescence sensibility with increasing dopant concentration. Thus, understanding the correlation of structural and luminescent properties is fundamental to optimizing a set of desired optical responses in these materials. Typically, lighting devices based on Eu^{3+}-doped UV-absorbing inorganic phosphors (*e.g.*, Y_2O_3:Eu^{3+}, YVO_4:Eu^{3+}, $CaTiO_3$:Eu^{3+}, YPO_4:Eu^{3+}, Ca_2ZnWO_6:Eu^{3+}, $LaPO_4$:Eu^{3+}, $GdAlO_3$:Eu^{3+}, $Ba_2CaZn_2Si_6O_{17}$:Eu^{3+}) are widely used for solid-state lighting [24–28].

In this scenario, our work proposes investigating and optimizing Eu^{3+}-doping concentrations in $BaMoO_4$ and $BaWO_4$ host matrices prepared by a soft chemistry coprecipitation method. This synthesis occurs in an aqueous medium; therefore, there is no need for additional steps to utilize other chemical reactants or special conditions (temperature or pressure control), resulting in NaCl as a by-product, without unwanted waste and low energy consumption. Furthermore, high crystalline purity $BaMO_4$:Eu^{3+} materials have been obtained. Here, we study the structural and photoluminescent behaviors based on the Rietveld refinement and theory of 4f–4f intensities, respectively. The experimental intensity parameters (Ω_λ) of luminescent materials were correlated with the chemical environment and polarizability around the Eu^{3+} ion. Besides, the intrinsic emission quantum efficiencies ($Q_{Eu^{3+}}^{Eu^{3+}}$) of the luminescent materials have been determined and discussed. The spectroscopic results suggest that the luminescent $BaMoO_4$:Eu^{3+} and $BaWO_4$:Eu^{3+} materials can be promising candidates for energy conversion and lighting applications.

2. Experimental

2.1. Preparation of $BaMO_4$:Eu^{3+} materials

All materials used in the syntheses were purchased from Sigma-Aldrich and Synth and used without further purification. The purity of the employed reagents is as follows: europium oxide 99.99%, barium chloride hexahydrate 99%, sodium tungstate 99%, sodium molybdate 99%, hydrochloric acid 37% (w/w). Firstly, $EuCl_3{\cdot}6H_2O$ precursor preparation was carried out by reacting Eu_2O_3 with concentrated hydrochloric acid (Supplementary material).

To prepare the $BaMO_4$:xmol%Eu^{3+} (M: Mo or W) materials (x = 2, 4, 6, 8 and 10 mol% Eu^{3+}) were used the aqueous solutions of $EuCl_3{\cdot}6\,H_2O$ (0.05 mol·L^{-1}), sodium tungstate or sodium molybdate (0.5 mol·L^{-1}) and $BaCl_2$ (0.45 mol·L^{-1}). Firstly, the barium chloride aqueous solution was added dropwise to the europium chloride aqueous solution under stirring. After, in this resulting solution, dropwise sodium tungstate or sodium molybdate solution was added at a rate of 1 mL·s^{-1}, stirring with the immediate formation of a white crystalline precipitate. It is worth mentioning that the precipitation occurs instantaneously due to the solubility product of $BaWO_4$ and $BaMoO_4$ are $K_{ps} = 3.5 \times 10^{-8}$ and $K_{ps} = 3.54 \times 10^{-8}$ (25 °C), respectively. The reactional system was maintained by vigorous magnetic stirring for 1 h. Next, the precipitate was filtered and washed several times until the presence of chloride was not detected in the filtrate by using an $AgNO_3$ solution. After all, the product was dried in a desiccator for 24 h under reduced pressure [29,30].

2.2. Instrumental

Structural analysis was performed by powder X-ray diffraction (PXRD) acquired by KαCu radiation on a Rigaku Miniflex II diffractometer within the 10–80º (2θ) range, using a 0.05º s^{-1} step width under 30 kV voltage and 15 mA current. FTIR spectral data were recorded on Agilent Cary 630 spectrometer in the spectral range from 650 to 4000 cm^{-1}. Raman spectra were recorded on a Renishaw inVia Raman Microscope, operating in confocal mode, the samples were excited with an excitation laser of wavelength, λ = 633 nm, and the signal was detected by a Renishaw CCD camera detector. In addition, Thermogravimetric analysis (TGA) was carried out in a Mettler Toledo-TGA/851 for the 30–700 ºC range with a 10 ºC min^{-1} heating rate under standard synthetic air (80% N_2 and 20% O_2) flux of 50 mL min^{-1}.

Scanning electron microscopy (SEM) images via Backscattered Electrons (BSE) were obtained on Tabletop Tescan Vega3-XMU with an 80 mm^2 Silicon Drift Detector (SDD) under 10 kV in high vacuum at room temperature, and Energy Dispersive Spectroscopy (EDS) data for elemental mapping imaging and characteristic X-ray emission spectra were recorded by an XFlash 430 H detector within the 0.4–10 keV energy range in a HITACHI TM3000 microscope under a 15 kV voltage in a BSE imaging setup. Transmission electron microscopy (TEM) and electron diffraction images were acquired on a JEOL JEM 2100 microscope with a LaB_6 filament under 200 kV voltage. Diffuse Reflectance Spectroscopy (DRS) measurements were performed on a Shimadzu UV-2600 spectrophotometer by an integrating sphere in the 220–800 nm spectral range with a 0.1 nm·s^{-1} step width, applying $BaSO_4$ as a standard reference.

Excitation and emission spectra were recorded on a HORIBA Fluorog-3 spectrofluorometer on an axial setup of 22.5° with a blazed holographic grating of 1200 lines/mm. They were registered by a photomultiplier (PMT) with a 0.2 nm s^{-1} step width. Furthermore, lifetime measurements were acquired using a pulse

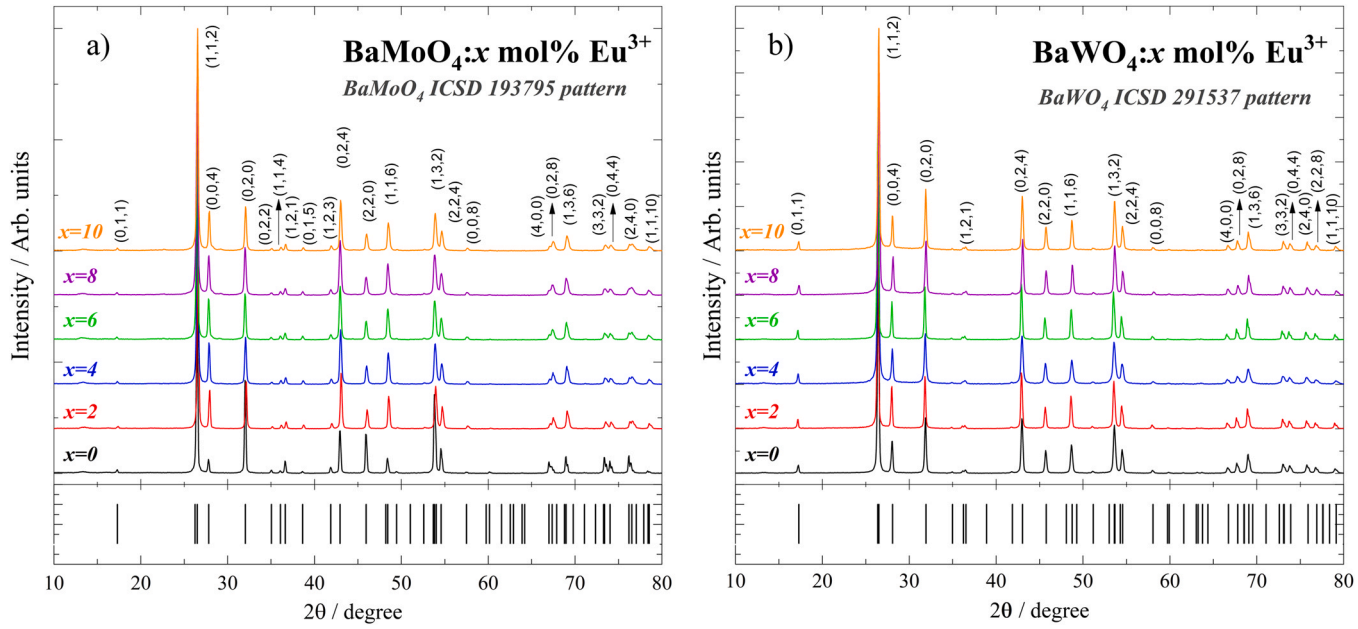

Fig. 1. X-ray powder diffraction patterns of the a) BaMoO4:xmol%Eu^{3+} and b) $BaWO_4$:xmol% Eu^{3+}, where x: 0, 2, 4, 6, 8 and 10 mol%. The I.C.S.D. standards for tetragonal $BaMoO_4$ (193795) and $BaWO_4$ (291537) are also presented.

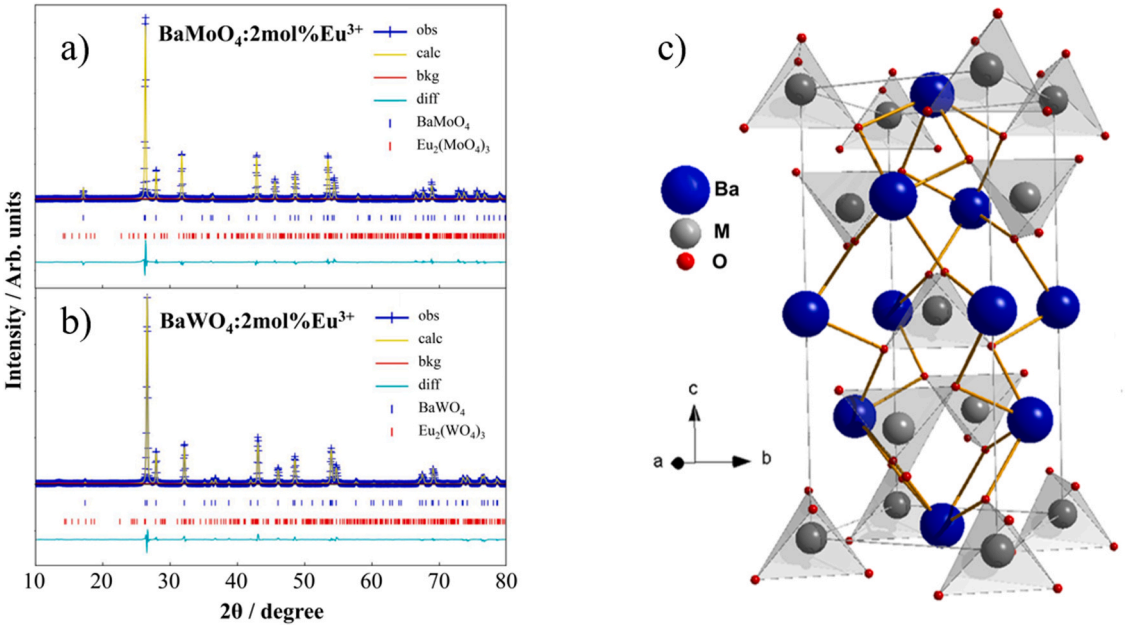

Fig. 2. Rietveld refinement of PXRD patterns for a) $BaMoO_4$:2% Eu^{3+}, b) $BaWO_4$:2% Eu^{3+} for tetragonal $BaMoO_4$ (193795), $BaWO_4$ (291537) and monoclinic $Eu_2(WO_4)_3$ (15877) and $Eu_2(MoO_4)_3$ (153371) I.C.S.D. standards, and c) Tetragonal scheelite-type unit cell $BaMO_4$ materials built on Diamond 4 software.

interval of 61 ms with a 0.05 ms step width, monitoring the Eu^{3+} (612 nm) characteristic emission under UV (394 nm) excitation.

3. Results and discussion

3.1. Structural analysis

The PXRD data suggest that Eu^{3+}-doping into $BaMoO_4$ host matrix directly affects the d_{hkl} (112)/(020), d_{hkl} (112)/(132), and d_{hkl} (112)/(220) intensity ratios compared to those from the undoped $BaMoO_4$ material (Fig. 1a), showing a significant decrease (~50%) in diffraction peak intensities of these reflections, as well as a sizable increase (~200%) for the d_{hkl} (112)/(004) ratio for Eu^{3+}-doped $BaMoO_4$ materials. This structural effect suggests that substitutional Eu^{3+} ions in Ba^{2+} sites may inhibit crystal growth in the < 112 > direction, while lower surface energies account for the growth in the < 004 > direction. These results corroborate with particle morphology controlled by high surface stability reported for the equivalent [112], [001], and [100] facets [30], as surface tension decreases with the number of uncoordinated atoms (relative to the bulk coordination number CN: 8) with only three oxygen atoms coordinated to each barium atom in the [112] and six oxygen atoms to [001] and [100] surfaces, respectively.

Such structural behavior is not observed for the $BaWO_4$: xmol% Eu^{3+} materials (Fig. 1b), as no significant changes in the diffraction peak intensity ratio, were noted with increasing Eu^{3+} content. This

Table 1
Rietveld refinement results for $BaMO_4$:xmol%Eu^{3+} compounds (M: W or Mo; x: 0%, 2%, 4%, 6%, 8% and 10%mol) by the $BaMO_4$ ICSD standards. Lattice parameters (a, b, c, α, β, γ, and V), reduced χ^2, R_{wp}, and R_{exp} values are also calculated.

Materials	$BaMO_4$	Lattice parameters				χ^2	R_{wp}	R_{exp}
	(%)	a = b (Å)	c (Å)	α = β = γ (deg.)	V (Å^3)	(%)	(%)	(%)
$BaWO_4$	100.00	5.6070	12.7101	90	399.592	1.640	10.46	6.38
$BaWO_4$:2 mol%Eu^{3+}	99.802	5.6129	12.7102	90	400.439	1.342	9.84	7.33
$BaWO_4$:4 mol%Eu^{3+}	97.745	5.6084	12.6934	90	399.257	1.334	9.48	7.11
$BaWO_4$:6 mol%Eu^{3+}	99.981	5.6110	12.7012	90	399.888	1.450	9.90	9.83
$BaWO_4$:8 mol%Eu^{3+}	99.082	5.6087	12.6960	90	399.383	1.377	9.67	7.02
$BaWO_4$:10 mol%Eu^{3+}	99.367	5.6074	12.7053	90	399.493	1.360	9.82	7.21
$BaMoO_4$	100.00	5.5803	12.8113	90	398.953	2.500	16.16	6.46
$BaMoO_4$:2 mol%Eu^{3+}	99.953	5.5761	12.7956	90	397.860	1.190	10.32	8.67
$BaMoO_4$:4 mol%Eu^{3+}	99.703	5.5773	12.7938	90	397.982	1.390	11.24	8.09
$BaMoO_4$:6 mol%Eu^{3+}	99.970	5.5769	12.7930	90	397.895	1.630	10.70	6.56
$BaMoO_4$:8 mol%Eu^{3+}	99.485	5.5781	12.7955	90	398.144	1.480	10.99	7.43
$BaMoO_4$:10 mol%Eu^{3+}	99.395	5.5771	12.7910	90	397.863	1.610	12.35	7.67

structural feature is attributed to more negligible distortion effects of the crystal lattice in these materials due to the larger $[WO_4]^{2-}$ group [30–32]. The substitution of Ba^{2+} by the Eu^{3+} ion necessitates charge compensation. In these materials, two Ba^{2+} sites are occupied by one Eu^{3+} ion, ensuring overall charge equilibrium compensating for the charge mismatch. Moreover, another possibility is the entrance of Na^{+} in Ba^{2+} sites would decrease the probability of the formation of other charge compensation defects, such as alkaline earth ion metal vacancies ($V_M^{''}$) or interstitial oxygen ($O_i^{''}$) as reported in reference [14,17,19]. For $BaMO_4$:Eu^{3+} (M: Mo and W) materials, ionic radii values of the scheelite-type crystal structure [e.g. Ba^{2+} (1.42 Å, CN:8), and Mo^{6+} (0.41 Å, CN: 4) or W^{6+} (0.42 Å, CN: 4)] indicate that dopant substitution e.g. Eu^{3+} (1.07 Å, CN: 8) occurs at pseudo-cubic Ba^{2+} sites [14,17,19].

Moreover, the lattice parameters and atomic positions of the crystalline structure were determined by the Rietveld refinement method (Fig. 2, Fig. S1). The calculated values and statistical parameters R_{exp}, R_{wp}, and χ^2 for the $BaMO_4$ structures (Table 1) indicated that these materials did not present significant phase segregation, suggesting that the Eu^{3+} ions were successfully incorporated into the $BaMO_4$ structure even at the highest europium doping concentrations.

Lattice parameter plots (Fig. S2) were constructed to investigate further the effect of increasing Eu^{3+} content from the undoped $BaMO_4$ matrices. As it can be seen from the Rietveld refinement, the lattice parameter values for the $BaWO_4$ material are in good accordance with the data reported in the literature (ICSD 291537). The crystallite size of $BaMO_4$:xmol%Eu^{3+} materials may also be understood by the increasing defect formation (*eg.* $V_{Ba}^{''}$) along Eu^{3+}-doping, as higher lattice strain typically inhibits crystallite size growth. The cell dimensions of the solid solution do not vary linearly with the Eu^{3+} concentration as the solute component, which does not strictly follow *Vegard's law* for this system [16,30–33].

All lattice parameter values of the $BaMoO_4$ matrix are slightly higher than those reported standards (ICSD 193795); however, they diminish significantly for $BaMoO_4$:xmol%Eu^{3+} materials. In addition, an increase of *a* or *b* parameters and a decrease of *c* values with higher doping concentrations are also observed. These results suggest structural distortions and point defects generated to accommodate the Eu^{3+} ions doped into the $BaMoO_4$ matrix [33]. On the other hand, the $BaWO_4$:xmol%Eu^{3+} materials present similar lattice parameter values, indicating minor distortions in the neighboring $[WO_4]^{2-}$ group [29].

In addition, it is highlighted that the characteristic diffraction peaks for the BaO, WO_3, MoO_3, and Eu_2O_3 compounds were not observed, as the Rietveld refinement analysis revealed only minimal amounts of $Eu_2(MO_4)_3$ by-products (< 1%). Besides, neither impurities from the $Na_2(MO_4)$ precursors nor phase segregation were identified, indicating high crystallographic purity for the prepared luminescent materials. The crystal structures of the $BaMO_4$:Eu^{3+}materials were generated from the Diamond 4 software (Fig. 2c), highlighting the tetragonal structure of molybdate and tungstate host matrices.

The average crystallite size was calculated by the Scherrer method given by expression (Eq. 1) [32].

$$D = \frac{K\lambda}{\beta \cos\theta} \quad (1)$$

where D is the average crystallite size, K is the shape factor, λ is the X-ray wavelength, and β is the line broadening at the full width at half maximum (FWHM) of the diffraction peaks of the $BaMO_4$:xmol% Eu^{3+} materials (Fig. 3), applying a NaCl pattern as a standard correction. Besides, the crystallite size was determined as a function of d_{hkl} (Fig. S3) by using several diffraction peaks, yielding an average crystallite size at ~30 nm (Table. S1).

$BaMoO_4$:xmol%Eu^{3+} materials show a significant size decrease trend (up to 8 nm) with increasing europium concentration in contrast to this, no significant effect on average crystallite size (≤ 3 nm) for the $BaWO_4$:xmol%Eu^{3+} materials was achieved. Such size effect is intrinsically linked with the previously discussed d_{hkl} intensity ratio and peak broadening identified in PXRD profiles. The average crystallite size decrease observed for $BaMoO_4$:Eu^{3+} materials with increasing Eu^{3+} concentration is assigned to the distortions in the crystal lattice caused by the difference in ionic radii [i.e., NC= 8: Ba^{2+}

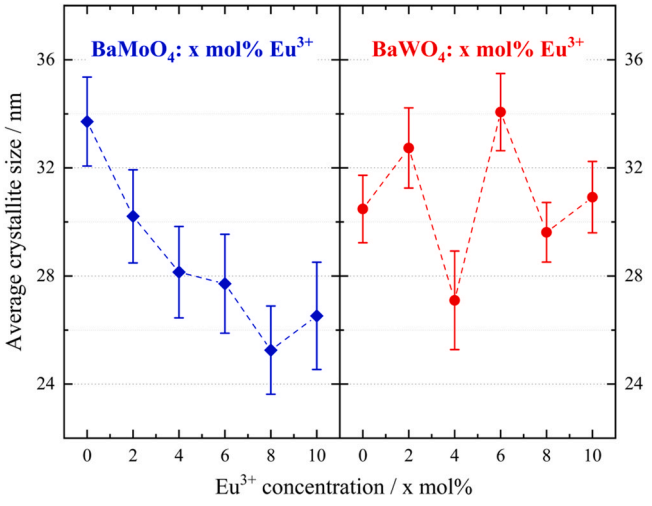

Fig. 3. Average crystallite size estimate for $BaMoO_4$ and $BaWO_4$ materials with increasing Eu^{3+} concentration with error analysis determined by standard deviation.

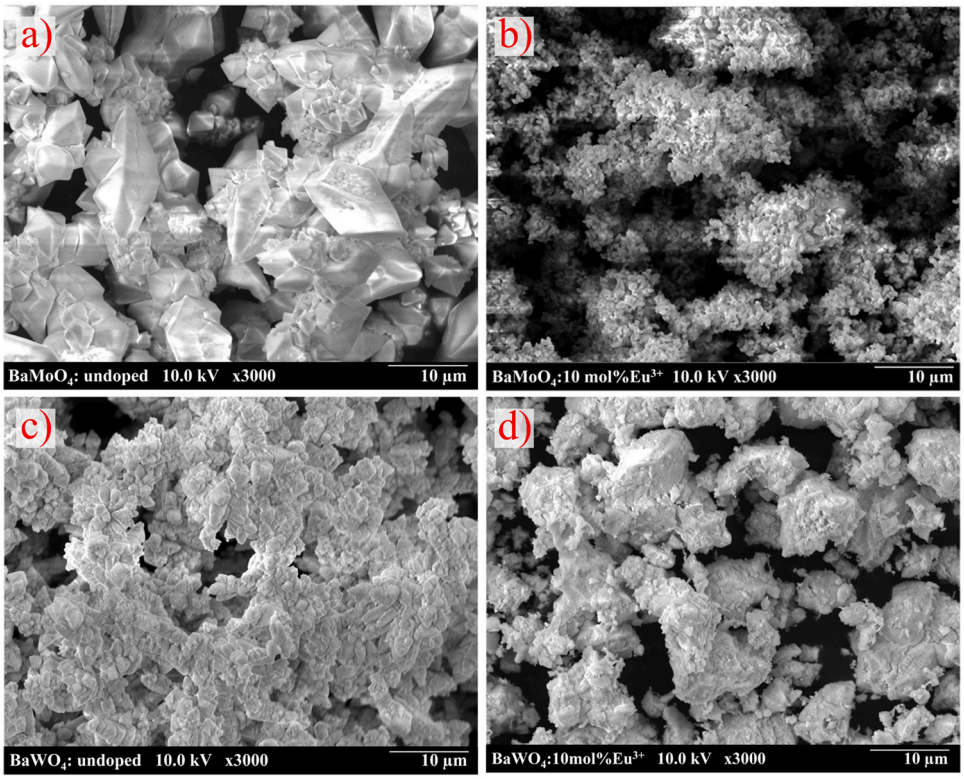

Fig. 4. S.E.M. images for a) $BaMoO_4$ and b) $BaMoO_4$:10 mol% Eu^{3+} c) $BaWO_4$, d) $BaWO_4$:10 mol% Eu^{3+}, acquired via B.S.E. under 10 kV.

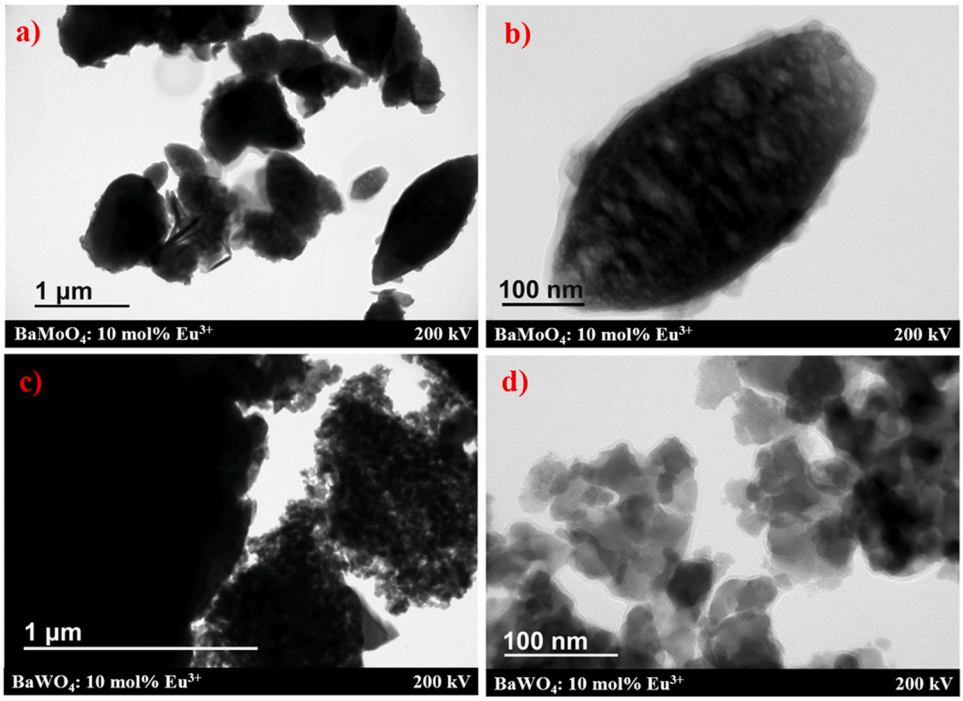

Fig. 5. Bright field TEM images for a-b) $BaMoO_4$:10 mol% Eu^{3+} and c-d) $BaWO_4$:10 mol% Eu^{3+} acquired under 200 kV.

= 142(8); Eu^{3+} = 107(8)]. Additionally, the size increase of WO_4^- tetrahedra for $BaWO_4$:Eu^{3+} materials may inhibit the decrease in crystallite size with increasing Eu^{3+} content.

SEM images present aggregates of micrometer-sized particles with an apparent size decrease for $BaMoO_4$:Eu^{3+} materials as the doping concentration increases, showing smaller particles on top of larger crystals (~10 µm). In contrast, undoped $BaWO_4$ and Eu^{3+}-doped $BaWO_4$ materials do not present such behavior, presenting mostly similar particle sizes. Therefore, quantitative average size estimate could not be confirmed based singly on SEM images due to large particle aggregates. For the $BaMoO_4$ matrix (Fig. 4a), the crystal growth in the < 112 > direction is identified for the characteristic tetragonal bipyramid-like morphology [30,34]. An increasing Eu^{3+} concentration (Fig. S4) results in more apparent (004) facets arising

from inhibited crystal growth (Fig. 4b), corroborating with the structural data presented by the PXRD results. On the other hand, the $BaWO_4$:xmol%Eu^{3+} material (Fig. 4c) shows characteristic morphology of exposed (112) facets due to an increase of surface energy for (100) and (001) [31] for x: 0, 2, and 4. In contrast, significant differences in the presence of small aggregates on top of larger polycrystalline are observed with Eu^{3+}-doping set at x: 6, 8, and 10 (Fig. S5), as $BaWO_4$:10 mol%Eu^{3+} exhibits the most radical change in surface morphology (Fig. 4d).

EDS elemental mapping images of the $BaMoO_4$:10 mol%Eu^{3+} (Fig. S6), and $BaWO_4$:10 mol%Eu^{3+} (Fig. S7) revealed a homogeneous distribution even with europium doping concentration set at 10 mol %, indicating successful Eu^{3+}-doping into both matrices. The characteristic X-ray emission spectra (Fig. S8) showed mainly the intense W($M_{\alpha1}$), and Mo ($L_{\alpha1}$) lines together with typical O($K_{\alpha1}$) emission, as the registered Ba ($L_{\alpha2}$; $L_{\beta1}$) signal has a significantly lower intensity. Still, a small amount of Sn ($L_{\beta1}$) impurities in $BaMoO_4$:10 mol%Eu^{3+} were also observed. Additionally, L emission lines of Eu in the 5.8–7.5 keV range were not observed in the spectra owing to the low X-ray emission intensity and the intense background noise of bremsstrahlung radiation [35].

Furthermore, TEM images (Fig. 5) supported the mentioned morphology characteristics of the prepared materials of bi-pyramidal-like sub-micron polycrystalline particles for both systems. However, it is noted that while the $BaMoO_4$:10 mol%Eu^{3+} material preserves its features illustrated at higher magnification images, presenting well-defined particles, the $BaWO_4$:10 mol%Eu^{3+} material exhibited a distinct behavior. Besides, much smaller particles (< 100 nm) were observed distributed on the surroundings of micrometric-sized crystals in a more pronounced way compared to the barium molybdate system.

Additionally, HRTEM images were also obtained, and it was possible to derive the crystallite size for both materials (Fig. S9) using the (004) and (112) reflections observed in electron diffraction patterns (Table S2). Therefore, it was recognized that the crystalline domains of the $BaMoO_4$:10 mol%Eu^{3+} material extended for around 30 nm. This result corroborates with the previously obtained average values by Scherrer's equation, where the $BaWO_4$:10 mol%Eu^{3+} compound presented coherent domains of up to about 50 nm, which may be accounted for variations in the shape factor due preferential crystal growth in this system.

FTIR spectra (Fig. S10) of the $BaMO_4$:xmol%Eu^{3+} materials show an intense absorption band at 800 cm^{-1} assigned to the stretching vibration mode (υ_{M-O}). Moreover, broad absorption bands are associated with stretching (υ_{O-H} ~3450 cm^{-1}) and bending (δ_{H-O-H} ~1630 cm^{-1}) vibrations originating from H_2O molecules adsorbed on the surface of polycrystalline particles are also observed [25,34]. The absorption bands at around 2360 and 1400 cm^{-1} in all materials may be attributed to $\upsilon_{O=C=O}$, and $\upsilon_{C=O}$ from CO_2, respectively. Raman spectra of the $BaMO_4$:xmol%Eu^{3+} (M: Mo or W) materials (Fig. 6), recorded in the range of 125–1000 cm^{-1}, exhibit intensity and similar lines. All the expected lines are observed in the Raman signal, presenting ten active vibrational modes ($3A_g$ + $4B_g$ + $3E_g$) as following (in cm^{-1}): $[MoO_4]^{2-}$ 890 (A_g), 837 (B_g), 791 (E_g), 358 (E_g), 344 (B_g), 326 (B_g), 191 (E_g) and 132 (B_g) and $[WO_4]^{2-}$ 924 (A_g), 829 (B_g), 793 (E_g), 352 (E_g), 344 (B_g), 332 (B_g), 191 (E_g) and 150 (B_g), which are characteristics of scheelite-type structure with tetragonal symmetry (C_{4h}^6) [36,37]. Additionally, no unusual bands or any significative changes were not observed, even when doping with different concentrations of the Eu^{3+} ion. Raman spectral results corroborate with those from the PXRD data.

Thermogravimetric curves (TG) of the undoped matrix, as well as doped $BaWO_4$:xmol%Eu^{3+} and $BaMoO_4$:xmol%Eu^{3+} (x: 2 and 10 mol %) materials, exhibit low weight loss event in the temperature interval from 35° to 250°C (Fig S11). This Thermal feature is attributed to the mass loss water molecules (absorption, adsorption, and crystallization), which agrees with the infrared data of the hydrate materials. After this dehydration event, the materials remain stable up to 700 °C, indicating good thermal stability of all materials at high temperatures.

3.2. Optical properties

Diffuse Reflectance Spectroscopy (DRS) data of $BaMO_4$:xmol% Eu^{3+} phosphors (Fig. 7a) mainly shows the broad reflectance band assigned to VB → CB transitions that are overlapped with the LMCT (O^{2-} → Mo^{6+}) band from 220 to 340 nm. Furthermore, it is observed the O^{2-} → Eu^{3+} LMCT transition (300–360 nm) and narrow absorption bands assigned to the $^7F_0$ → $^5D_1$, $^5D_2$, $^5D_3$, $^5L_6$, $^5G_2$, $^5G_5$,$^5G_6$ and $^5D_4$ transitions of the Eu^{3+} ion (360–550 nm) in the $BaMO_4$:xmol% Eu^{3+} materials [23]. The $BaWO_4$:xmol%Eu^{3+} (Fig. 7b) shows the highest reflectance intensity band at 225 nm which is assigned to transition between the valence band to the conduction band (VB → CB) of the host matrix. This represents the main absorption processes of the $BaWO_4$ matrix and $BaWO_4$:2 mol%Eu^{3+} materials, overlapping with the LMCT broad bands in the spectral region from 270 to 300 nm. As Eu^{3+}-doping concentration increases, the LMCT (O^{2-} → W^{6+} and O^{2-} → Eu^{3+}) [16,38] transitions become more apparent as a redshift on the broad absorption band is observed. These optical phenomena are related to absorption processes originating from meta-stable states (W^{5+} and Eu^{2+}), which may give rise to collective emission processes derived from the host matrix and/or Eu^{3+} ions. It is noteworthy that the absorptions by the tungstate and molybdate have high absorption coefficients.

It is noteworthy that the band gap energies (E_g) of the barium molybdate and tungstate matrices were calculated by the single-constant Kubelka-Munk function [$F(R_\infty)$] (Eq. 2) [39–42] from DRS spectra, where K and S represent the material's absorption and scattering coefficients, given by $(1 - R_\infty)$ and $2R_\infty$ respectively, while R_∞ corresponds to the experimentally measured reflectance, and n stands for the transition constant, assuming values of 0.5 or 2 for direct and indirect allowed transitions accordingly. Furthermore, h corresponds to Planck's constant and v to the photon's frequency. To find the experimental band gap energy, a linear fit of $F(R_\infty) \rightarrow 0$ was plotted. Its intersection with the energy axis represents E_g for these matrices (Fig. S12 and Fig. S13). The calculated values from the E_g transitions (Table S3) corroborate with data previously reported in the literature [15,38], as the statistical parameters of coefficient of determination (R^2) and residual sum of squares (RSS) presented appropriate values for a high-precision linear fitting for extrapolation of the single-constant Kubelka-Munk curves [40].

$$[F(R_\infty)hv]^{1/n} = [(K/S)hv]^{1/n} \quad (2)$$

Interestingly, the energy band gap of the $BaMoO_4$:xmol%Eu^{3+} shows only slight variations in their values with increasing europium concentration, as the LMCT bands do not show a substantial shifting compared to the VB → CB band of the $BaMoO_4$ matrix [41], varying from 4.35 to 4.45 eV for x:0–10 mol%. In contrast, the calculated E_g values for $BaWO_4$:xmol%Eu^{3+} present a significant spectral shift in the UV region from 5.18 to 4.30 eV for x: 0–10 mol%. For instance, the $BaWO_4$:2 mol%Eu^{3+} material shows a high E_g value, similar to the undoped $BaWO_4$ matrix due to its predominant VB → CB direct allowed electronic transitions. On the other hand, in $BaWO_4$:xmol%Eu^{3+} materials (x: 4, 6, 8, and 10) the LMCT band redshifts decreasing E_g values to around 4.3 eV, which may be due to the overlapping of the O^{2-} → W^{6+} and O^{2-} → Eu^{3+} bands [17,26,43].

3.3. Luminescence properties

Excitation spectra of the $BaMoO_4$:xmol%Eu^{3+} (Fig. 8a) and $BaWO_4$:xmol%Eu^{3+} (Fig. 8b) materials exhibit characteristic narrow

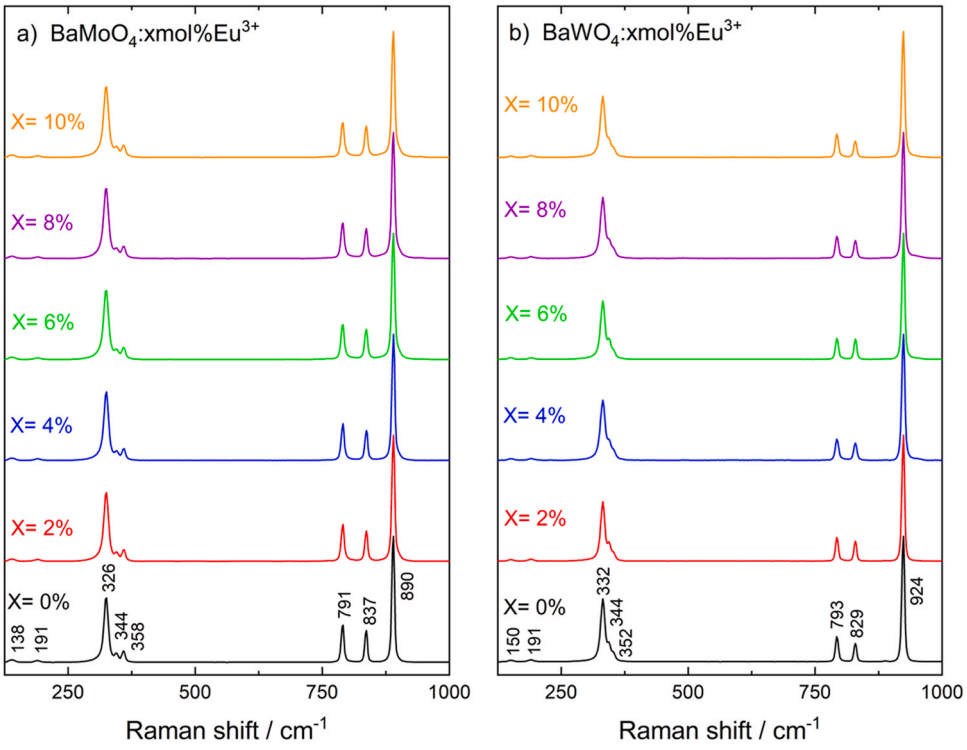

Fig. 6. Raman scattering spectra of the a) BaMoO4:xmol%Eu^{3+} and b) $BaWO_4$:xmol% Eu^{3+} materials, where x: 0, 2, 4, 6, 8 and 10 mol%.

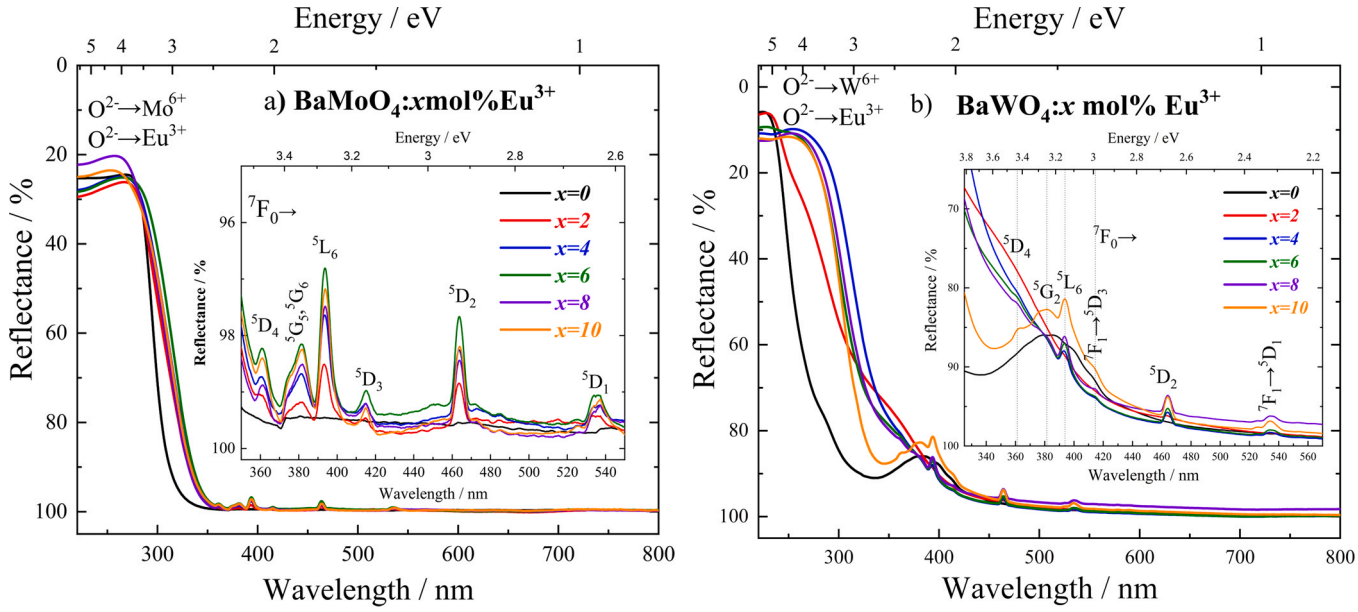

Fig. 7. DRS spectra of a) $BaMoO_4$:x mol% Eu^{3+} and b) $BaWO_4$:xmol%Eu^{3+} materials, where x: 0, 2, 4, 6, 8 and 10 mol%. Inserts present Eu^{3+} intraconfigurational transitions in the UV-Vis range are amplified.

Eu^{3+} absorption bands assigned to $^7F_0 \rightarrow {}^5D_4$ (362 nm), $^5G_2$ (381 nm), $^5L_6$ (394 nm), $^5D_3$ (415 nm), $^5D_2$ (464 nm) and $^5D_1$ (534 nm) transitions [23]. Similar spectral profiles for the molybdate system with increasing Eu^{3+} doping concentration are observed, in contrast to Eu^{3+}-doped tungstate materials [43–45]. Based on the deconvolution curves for the LMCT bands, the contribution of $O^{2-} \rightarrow Mo^{6+}$ and $O^{2-} \rightarrow Eu^{3+}$ transitions, there are no significant changes with an increasing Eu^{3+} concentration in the $BaMoO_4$ matrix (Fig. 8a, Fig. S14). Also, a relatively low absorption intensity of these bands compared to $4f^6$-$4f^6$ transitions was recorded. Conversely, the deconvolution curves for $BaWO_4$:xmol%Eu^{3+} materials present a significant redshift of the LMCT bands, mainly due to the contribution of europium $O^{2-} \rightarrow Eu^{3+}$ transition (Fig. 8b, Fig. S14) [17]. It is also noticeable that the LMCT band intensities decrease compared to the $4f^6$-$4f^6$ transitions from 2 to 10 mol% concentrations, indicating that the direct excitation from Eu^{3+} ions is also operative.

Emission spectra of $BaMoO_4$:xmol%Eu^{3+} (Fig. 9a) and $BaWO_4$:xmol%Eu^{3+} (Fig. 9b) phosphors exhibit the narrow bands from the Eu^{3+} ($^5D_0 \rightarrow {}^7F_{0-4}$) transitions with the highest red luminescence intensity assigned to the hypersensitive $^5D_0 \rightarrow {}^7F_2$ transition [23]. Moreover, very weak emission bands from the $^5D_1$ level [44,45] could be observed, suggesting that multiphonon non-radiative decay

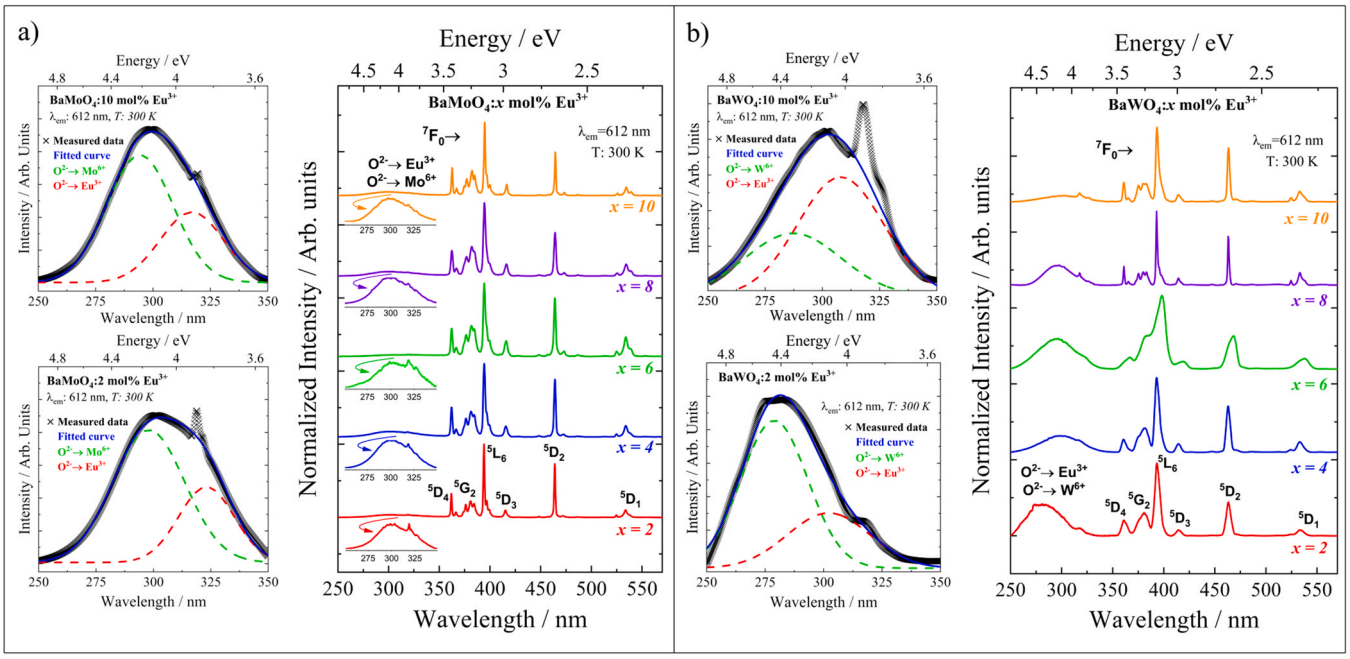

Fig. 8. Excitation spectra of a) $BaMoO_4$:xmol%Eu^{3+} and b) $BaWO_4$:xmol%Eu^{3+} materials, where x: 0, 2, 4, 6, 8 and 10 mol, monitored at 612 nm emission.

from this level is not very operative, even at room temperature [46,47] (inset in Fig. 9). Furthermore, a remarkable $[WO_4]^{2-}$ broad emission band at 450 nm [15] was observed for the $BaWO_4$:xmol% Eu^{3+} system (Fig. 9b), mainly for x: 6, and 8 mol%, while no significant emission bands from the $[MoO_4]^{2-}$ group was noted for $BaMoO_4$:xmol%Eu^{3+} materials.

The $^5D_0 \rightarrow {}^7F_{0-4}$ emission bands of the $BaWO_4$:xmol%Eu^{3+} materials (x: 4, 6, 8, and 10) showed a significant broadening in their spectral profiles with increased Eu^{3+} concentration (Fig. 9b). This optical result suggests different symmetry sites around europium ion. In contrast, the molybdate system shows similar spectral profiles at different Eu^{3+} concentrations from 2 to 10 mol%, maintaining their characteristic narrow emission $^5D_0 \rightarrow {}^7F_{0-4}$ bands (Fig. 9a).

Luminescence decay curves of the main emitting level ($^5D_0$) from the Eu^{3+} ion were monitored at 612 nm under 394 nm excitation for all Eu^{3+}-doped materials (Figs. S15 and S16). The lifetime (τ) values (Table 2) determined for $BaMoO_4$:xmol%Eu^{3+} materials (Fig. S15) show similar results of around 0.53 ms. On the other hand, the $BaWO_4$:xmol%Eu^{3+} system (Fig. S16) demonstrated a slight decrease of (τ_{AV})values with increasing doping concentration (from 0.64 to

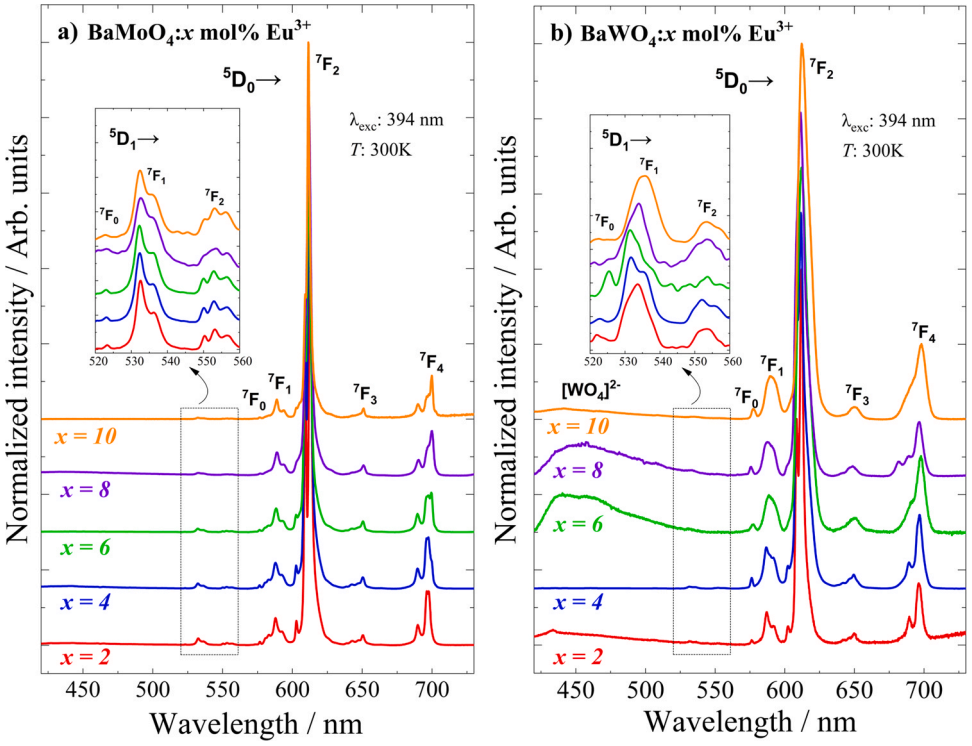

Fig. 9. Emission spectra of (a) $BaMoO_4$:xmol%Eu^{3+} and (b) $BaWO_4$:xmol%Eu^{3+} materials, where x: 0, 2, 4, 6, 8 and 10 mol under 394 nm excitation.

Table 2
Experimental intensity parameters (Ω_λ), average lifetime (τ_{av}), radiative (A_{rad}) and non-radiative (A_{nrad}) coefficients, and intrinsic quantum yield ($Q^{Eu^{3+}}_{Eu^{3+}}$) values for $BaMoO_4$:xmol%Eu^{3+} and $BaWO_4$:xmol%Eu^{3+} materials (x: 2, 4, 6, 8 and 10 mol%).

Luminescent materials	Ω_2 (10^{-20} cm^2)	Ω_4 (10^{-20} cm^2)	τ_{av} (ms)	A_{rad} (s^{-1})	A_{nrad} (s^{-1})	$Q^{Eu^{3+}}_{Eu^{3+}}$ (%)
$BaMoO_4$:(2 mol%)Eu^{3+}	15	5	0.55	1232	641	68
$BaMoO_4$:(4 mol%)Eu^{3+}	16	6	0.49	1302	606	64
$BaMoO_4$:(6 mol%)Eu^{3+}	17	6	0.50	1330	745	67
$BaMoO_4$:(8 mol%)Eu^{3+}	17	6	0.58	1347	432	79
$BaMoO_4$:(10 mol%)Eu^{3+}	17	8	0.55	1434	446	79
$BaWO_4$:(2 mol%)Eu^{3+}	15	7	0.64	1193	513	77
$BaWO_4$:(4 mol%)Eu^{3+}	13	5	0.62	984	782	61
$BaWO_4$:(6 mol%)Eu^{3+}	9	4	0.51	777	1455	40
$BaWO_4$:(8 mol%)Eu^{3+}	9	3	0.52	714	1533	37
$BaWO_4$:(10 mol%)Eu^{3+}	13	6	0.49	1040	1307	51

0.49 ms). We attribute this decrease in (τ_{AV}) to the considerable increase in the non-radiative decay rate as displayed in Table 2, in contrast to the case of the molybdate materials. In the present case, cross-relaxation processes between Eu^{3+} ions do not interfere in the $^5D_0$ average lifetime. Moreover, based on the decay curves, we have not found evidence of energy migration trapping in the fast-diffusion regime at these europium doping concentrations.

These decay curves were well adjusted to bi-exponential functions, leading to the values of the pre-exponential terms (A_1 and A_2 coefficients) that are given in the Table S4. The average lifetimes (τ_{AV}) of the emitting $^5D_0$ level were calculated according to the Eq. 3 [48].

$$\tau_{AV} = \frac{(A_1\tau_1^2 + A_2\tau_2^2)}{(A_1\tau_1 + A_2\tau_2)} \quad (3)$$

Experimental intensity parameters Ω_2 (more sensitive to the angular part of the odd component of the ligand field) and Ω_4 (more sensitive to distance – covalency effects) of Eu^{3+} [49] were calculated from the luminescence spectra recorded under 394 nm excitation (Table 2). As the emission intensity (in terms of emitted number of photons) is given by $I_{0\to J} = A_{0\to J}N_o$, where $A_{0\to J}$is the spontaneous emission coefficient and N_0corresponds to the population of the emitting $^5D_0$ level. Thus, for experimental determination of $A_{0\to J}$values (Eq. 4), the allowed magnetic dipole transition ($^5D_0 \to {}^7F_1$) is used as a standard reference [50].

$$A_{0\to J} = \left(\frac{S_{0\to J}}{S_{0\to 1}}\right)A_{0\to 1} \quad (4)$$

where $S_{0\to J}$ is the integrated intensity of the corresponding $^5D_0 \to {}^7F_J$ transition. Hence, $\Omega_{2,4}$ values reported in Table 2 were calculated from Eq. 5 [50].

$$A_{0\to J} = \frac{4e^2\omega^3}{3hc^3}\frac{1}{2J+1}\chi\sum_{\lambda=2,4}\Omega_\lambda\langle {}^5D_0\|U^{(\lambda)}\|{}^7F_J\rangle^2 \quad (5)$$

where ω is the angular frequency of the $^5D_0 \to {}^7F_J$ transition, $\chi = \frac{n_0(n_0^2+2)^2}{9}$ represents the Lorentz local field correction factor, $n_0$corresponds to the refractive index of the material and the squared reduced matrix element values 0.0032 and 0.0023 for J = 2 and 4, respectively, were taken from reference [51]. It is worth mentioning that since the squared reduced matrix element for the $^5D_0 \to {}^7F_6$ transition is very small (U^6 = 0.0002) compared to the $^5D_0 \to {}^7F_2$ and $^5D_0 \to {}^7F_4$ transitions, the total contribution of the $^5D_0 \to {}^7F_6$ transition for the total spontaneous emission is very low. Consequently, the contribution of the radiative rate assigned to the $^5D_0 \to {}^7F_6$ transition for the intrinsic quantum yield values should be negligible. Furthermore, the total spontaneous emission $A_{rad} = \Sigma A_{0\to J}$ and intrinsic quantum yield is given by $Q^{Eu^{3+}}_{Eu^{3+}} = A_{rad}/A_{total}$ (where$A_{total} = 1/\tau = A_{rad} + A_{nrad}$) [50,52] (Table 2).

The similar Ω_2 values (~16 ×10^{-20} cm^2) and Ω_4 values (~6 ×10^{-20} cm^2) for the $BaMoO_4$:xmol%Eu^{3+} (x: 2–10) indicate no significant changes in the first coordination spheres around the europium ion (Table 2). On the other hand, the Ω_2 and Ω_4 values for the $BaWO_4$:xmol%Eu^{3+} materials are noticeably different (decrease) for Eu^{3+} concentrations of 6 and 8 mol%, suggesting structural changes in the tungstate system. [49,53]. This observed fact is clearly correlated with the accompanying decrease in the respective values of the radiative decay rates A_{rad} (Table 2).

The intrinsic emission quantum yield value ($Q^{Eu^{3+}}_{Eu^{3+}}$: 77–37%) of the Eu-doped $BaWO_4$ materials (Table 2) are consistent with the luminescence quenching due to the significantly higher non-radiative decay contributions for contents of 6, 8, and 10 mol%. In contrast, the $Q^{Eu^{3+}}_{Eu^{3+}}$ values of the $BaMoO_4$:xmol%Eu^{3+} materials show no significant changes (~70%). Therefore, the molybdates present a highly efficient luminescence independent of Eu^{3+} concentrations. It is noteworthy that the tungstate system at lower europium content (2 mol%) shows high intrinsic quantum efficiency (77%).

CIE (*Commission Internationale de l'Éclairage*) diagrams of the $BaMoO_4$:Eu^{3+} materials illustrated in Fig. 10a [54] display a slight redshift (high monochromatic character) in *x,y* coordinates as a function of increasing Eu^{3+} concentration (Table S5). Color coordinates were calculated by using the direct emission spectrum inputs of free format spectrum (wavelength versus emission

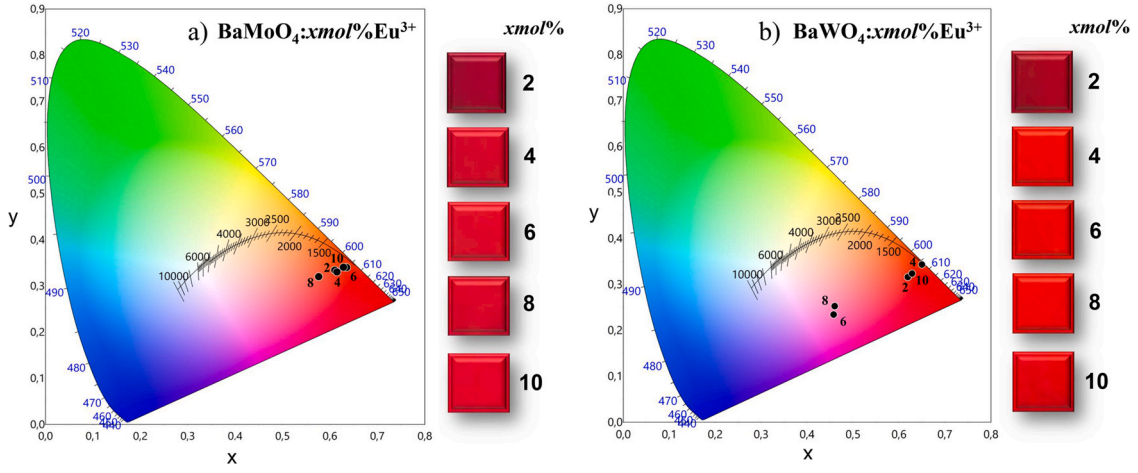

Fig. 10. C.I.E. diagram of luminescent materials a) $BaMoO_4$:xmol%Eu^{3+} and b) $BaWO_4$:xmol%Eu^{3+}, where x: 2, 4, 6, 8, and 10 mol%, under 394 nm excitation, respectively. Photographs of the materials taken with a digital camera under a 360 nm U.V. lamp are also shown.

intensity) for the luminescence spectra of $BaMO_4$:Eu^{3+} materials on the ColorCalculator 7.23 (OSRAM Sylvania, Inc.) software, plotted onto a CIE 2015 10° x,y diagram format. In comparison, the $BaWO_4$:mol%Eu^{3+} materials (Fig. 10b) show the narrow red emission bands of Eu^{3+} ion as well as the contribution of the broad emission band assigned to the $[WO_4]^{2-}$ group [19], exhibiting pronounced blueshift effects in the $BaWO_4$ matrix for concentrations of 6 and 8 mol% (Fig. 10b). This blueshift is clearly due to the very broad and asymmetric emission band centered around 450 nm (Fig. 8) whose tail extends considerably towards the lower energy side slightly overlapping the $^5D_0$ emitting level. This fact possibly induces a non-radiative back energy transfer involving the $^5D_0$ and the $^7F_1$ levels which might be responsible for the decrease of the average $^5D_0$ lifetime and the decrease of $Q_{Eu^{3+}}^{Eu^{3+}}$. Notice that this very broad emission band is not observed in the case of the molybdate materials. Its origin is unclear, but it could be due to the Stokes shift from the band observed around 390 nm in the reflectance spectra. Defects nearby the Eu^{3+} ion in the case of the tungstate material could be the reason. A further detailed investigation is needed.

4. Conclusions

In summary, highly crystalline Eu^{3+}-doped $BaMO_4$ luminescent materials (M: Mo or W) were successfully obtained by the coprecipitation method in an aqueous solution at room temperature (~300 K). Furthermore, this preparation method drastically reduces time and energy costs compared to ceramic, Pechini, and microwave preparation methods, which can be classified in at least six of the 12 principles of green chemistry. PXRD and Raman data confirmed the formation of a characteristic and highly crystalline scheelite-type structure for both materials, while SEM images revealed the formation of particle aggregates on top of the more prominent and well-defined crystalline surfaces with increasing Eu^{3+} concentrations.

The spectroscopic properties of these materials are significantly influenced by the LMCT excitation bands ($O^{2-} \rightarrow Mo^{6+}$, W^{6+}, and Eu^{3+}) as well as their intense red emission bands assigned to Eu^{3+} transitions. It was observed that the Ω_2 values are much higher than the Ω_4 values. This result is related to the fact that the $^5D_0 \rightarrow {}^7F_2$ transition presents a much higher intensity than $^5D_0 \rightarrow {}^7F_1$ one suggesting a low local symmetry around the Eu^{3+} ion, which might be due to angular distortions in the local coordination geometry. Interestingly, the $BaMoO_4$:xmol%Eu^{3+} (x: 8 and 10) and $BaWO_4$:2 mol %Eu^{3+} materials show the highest intrinsic quantum efficiencies values. Besides, the brightness is certainly assured by the high absorption coefficient of the tungstate and molybdate groups and efficient intramolecular energy transfer. Therefore, these luminescent materials prepared by the coprecipitation method are promising candidates for UV-Visible energy conversion.

CRediT authorship contribution statement

Renan P. Moreira: Conceptualization, Methodology, Investigation, Writing - original draft. **Leonardo H. C. Francisco:** Investigation, Data Curation, Writing - review & editing **Israel F. Costa:** Data curation, Visualization. **Helliomar P. Barbosa:** Data Curation, Visualization, Writing - review & editing, **Ercules E. S. Teotonio:** Data curation, Visualization, Writing - review & editing **Maria C. F. C. Felinto:** Conceptualization, Resources, Project administration, Writing - review & editing. **Oscar L. Malta:** Formal analysis, Writing - review & editing. **Hermi F. Brito**: Supervision, Writing - review & editing.

Data availability

Data will be made available on request.

Declaration of Competing Interest

The authors declare that they have no known competing financial interests or personal relationships that could have appeared to influence the work reported in this paper.

Acknowledgements

The authors thank the support given by the Brazilian Research Unity in Astrobiology - NAP/Astrobio for the Raman spectra acquisition and the Center for Lasers and Applications' Multiuser Facility at Nuclear and Energy Research Institute (CLA/IPEN) for carrying out the SEM/EDS experiments and the funding provided by the Brazilian Agencies FAPESP, CAPES, CNPq, and CNEN.

Appendix A. Supporting information

Supplementary data associated with this article can be found in the online version at doi:10.1016/j.jallcom.2022.168408.

References

[1] J.G. Bünzli, Trends Chem. (2019) 1.
[2] B. Zheng, J. Fan, B. Chen, X. Qin, J. Wang, F. Wang, R. Deng, X. Liu, Chem. Rev. 122 (2022) 5519.
[3] A. Bednarkiewicz, J. Drabik, K. Trejgis, D. Jaque, E. Ximendes, L. Marciniak, Appl. Phys. Rev. 8 (2021) 011317.
[4] J.F.C.B. Ramalho, A.N. Carneiro Neto, L.D. Carlos, P.S. André, R.A.S. Ferreira, Handb. Phys. Chem. Rare Earths (2022).
[5] J. Miranda De Carvalho, C.C.S. Pedroso, I.P. Machado, J. Hölsä, L.C.V. Rodrigues, P. Głuchowski, M. Lastusaari, H.F. Brito, J. Mater. Chem. C. 6 (2018) 8897.
[6] J.G. Bünzli, S.V. Eliseeva, P. Hänninen, H. Härmä (Eds.), Springer, Berlin. Heidelberg, 2010, pp. 1–45.
[7] S. Cho, J. Korean Phys. Soc. 69 (2016) 1479.
[8] B. Saravanakumar, S.P. Ramachandran, G. Ravi, V. Ganesh, A. Sakunthala, R. Yuvakkumar, Appl. Phys. A 125 (2019) 1.
[9] S.M.H.A. Sobhani-nasab, J. Mater. Sci. Mater. Electron. 27 (2016) 7548.
[10] I.L.V. Rosa, A.P.A. Marques, M.T.S. Tanaka, D.M.A. Melo, J. Fluor. 18 (2008) 239.
[11] R. Paradiso, S. Proietti, F.R. Far, J. Plant Growth Regul. 41 (2022) 742.
[12] K.N. Kumar, G. Kang, J. Lim, J. Choi, Inorg. Chem. 61 (2022) 3851.
[13] K.N. Kumar, L. Vijayalakshmi, P. Hwang, A.D. Wadhwani, J. Choi, J. Alloy. Compd. 840 (2020) 155589.
[14] R.D. Shannon, Acta Cryst. A32 (1976) 751.
[15] S.K. Stephen, S. Ganesh, T. Varghese, Radiat. Phys. Chem. 180 (2021) 109317.
[16] H. Wu, J. Peng, H. Sun, Q. Ruan, H. Dong, Y. Jin, Z. Sun, Y. Hu, Chem. Eng. J. 432 (2022) 134339.
[17] H.P. Barbosa, J. Kai, I.G.N. Silva, L.C.V. Rodrigues, M.C.F.C. Felinto, J. Hölsä, H.F. Brito, J. Lumin. 170 (2016) 736.
[18] J. Liu, A.M. Kaczmarek, R. Van Deun, Chem. Soc. Rev. 47 (2018) 7225.
[19] L.D.S. Alencar, A. Mesquita, C.A.C. Feitosa, R. Balzer, L.F.D. Probst, D.C. Batalha, M.G. Rosmaninho, H.V. Fajardo, M.I.B. Bernardi, Ceram. Int. 43 (2017) 4462.
[20] L. Wang, Y. Ma, H. Jiang, Q. Wang, C. Ren, X. Kong, J. Shi, J. Wang, J. Mater. Chem. C. 2 (2014) 4651.
[21] D. Yue, Q. Li, W. Lu, Q. Wang, M. Wang, C. Li, L. Jin, Y. Shi, Z. Wang, J. Hao, J. Mater. Chem. C. 3 (2015) 2865.
[22] M. Guzik, E. Tomaszewicz, Y. Guyot, J. Legendziewicz, G. Boulon, J. Mater. Chem. C. 3 (2015) 8582.
[23] K. Binnemans, Coord. Chem. Rev. 295 (2015) 1.
[24] G.B. Nair, H.C. Swart, S.J. Dhoble, Prog. Mater. Sci. 109 (2020) 100622.
[25] E.L. Gaiollo, R.P. Moreira, M.C.F.C. Felinto, E.E.S. Teotonio, H.P. Barbosa, H.F. Brito, 31 (2020) 2430.
[26] H.P. Barbosa, I.G.N. Silva, M. Claudia, F.C. Felinto, E.E.S. Teotonio, H.F. Brito, J. Alloy. Compd. 696 (2017) 820.
[27] K.V. Dabre, S.J. Dhoble, J. Lumin. 150 (2014) 55.
[28] J. Downloaded, S.A.O. Paulo, M. Guzik, E. Tomaszewicz, Y. Guyot, J. Legendziewicz, G. Boulon, 2015, 8582.
[29] E. L, M.S. L, L.S. Cavalcante, F.M.C. Batista, M.A.P. Almeida, A.C. Rabelo, I.C. Nogueira, N.C. Batista, J.A. Varela, a M.R.M.C. Santos, RSC Adv. 2 (2012) 6438.
[30] M.C. Oliveira, L. Gracia, C. Nogueira, M.F.C. Gurgel, J.M.R. Mercury, E. Longo, J. Andrés, 644 (2016) 634.
[31] M.C. Oliveira, L. Gracia, I.C. Nogueira, M.F. do, C. Gurgel, J.M.R. Mercury, E. Longo, J. Andrés, Ceram. Int. 42 (2016) 10913.
[32] H.P. Klug, L.E. Alexander, X-Ray Diffraction Procedures for Polycrystalline and Amorphous Materials, Wiley, New York, 1974.

[33] I.C. Nogueira, L.S. Cavalcante, P.F.S. Pereira, M.M. Jesus, J.M. Rivas, J. Appl. Crystallogr. 46 (2013) 1434.
[34] M. Ghaed-Amini, M. Bazarganipour, M. Salavati-Niasari, K. Saberyan, Trans. Nonferrous Met. Soc. China 25 (2015) 3967.
[35] A. Thompsom, D. Attwood, E. Gullikson, M. Howells, K.-J. Kim, J. Kirzs, J. Kortright, I. Lindau, A. Liu, P. Pianetta, A. Robinson, J. Scofield, J. Underwood, G. Williams, H. Winick, *X-Ray Data Booklet*, Lawrence Berkeley National Laboratory, University Of California, Berkeley, CA, 2009.
[36] T.T. Basiev, A.A. Sobol, Y.K. Voronko, P.G. Zverev, Opt. Mater. (Amst.) (*15*) (2000) 205.
[37] S.P.S. Porto, J.F. Scott, Phys. Rev. 157 (1967) 716.
[38] V. Mishra, M.K. Warshi, A. Sati, A. Kumar, V. Mishra, Mater. Sci. Semicond. Process 86 (2018) 151.
[39] H.R. Kang, Computational Color Technology, SPIE—The International Society For Optical Engineering, Bellingham, Washington-USA, 2006.
[40] B.D. Viezbicke, S. Patel, B.E. Davis, D.P.B. Iii, Phys. Status Solidi B 1710 (2015) 1700.
[41] J.C. Sczancoski, L.S. Cavalcante, N.L. Marana, R.O. Silva, R.L. Tranquilin, M.R. Joya, P.S. Pizani, J.A. Varela, J.R. Sambrano, M.S. Li, E. Longo, J. Andrés, Curr. Appl. Phys. 10 (2010) 614.
[42] M. Luo, X. Sha, B. Chen, X. Zhang, H. Yu, X. Li, J. Zhang, S. Xu, Y. Cao, Y. Wang, X. Wang, Y. Zhang, D. Gao, L. Wang, J. Am. Ceram. Soc. 105 (2022) 3353.
[43] C.A. Kodaira, H.F. Brito, O.L. Malta, O.A. Serra, J. Lumin. 101 (2003) 11.
[44] F. Chun, W. Deng, B. Zhang, W. Li, M. Xie, C. Luo, W. Yang, Ceram. Int. 46 (2020) 27238.
[45] D. Pi, F. Wang, X. Fan, M. Wang, Y. Zhang, Spectrochim. Acta - Part A Mol. Biomol. Spectrosc 61 (2005), p. 2455.
[46] J. Suda, P.G. Zverev, Vib. Spectrosc. 62 (2012) 85.
[47] A.K. Soni, A. Kumari, V.K. Rai, Sens. Actuators, B Chem. 216 (2015) 64.
[48] F.P. Aguiar, I.F. Costa, J.G.P. Espínola, W.M. Faustino, J.L. Moura, H.F. Brito, T.B. Paolini, M.C.F.C. Felinto, E.E.S. Teotonio, J. Lumin. 170 (2016) 538.
[49] A.N. Carneiro Neto, E.E.S. Teotonio, G.F. de Sá, H.F. Brito, J. Legendziewicz, L.D. Carlos, M.C.F.C. Felinto, P. Gawryszewska, R.T. Moura, R.L. Longo, W.M. Faustino, O.L. Malta, Handb. Phys. Chem. Rare Earths (2019) 55–162.
[50] H. Felinto Brito, O. Manoel Loureiro Malta, M. Claudia França Cunha Felinto, E. Epaminondas de Sousa Teotonio, Z. Rappoport (Ed.), PATAI'S Chem. Funct. Groups, John Wiley & Sons, Ltd, Chichester, UK, 2010.
[51] H.M. Carnall, W.T.; Crosswhite, H.; Crosswhite, Energy Level Structure and Transition Probabilitiesof the Trivalent Lanthanides in LaF3, 1977.
[52] Y. Tian, B. Chen, R. Hua, J. Sun, L. Cheng, H. Zhong, X. Li, J. Zhang, Y. Zheng, T. Yu, L. Huang, H. Yu, J. Appl. Phys. 109 (2011) 053511.
[53] R.T. Moura, A.N. Carneiro Neto, R.L. Longo, O.L. Malta, J. Lumin. 170 (2016) 420.
[54] N.C. George, K.A. Denault, R. Seshadri, Annu. Rev. Mater. Res. 43 (2013) 481.